Available online at www.sciencedirect.com
SCIENCE DIRECT®
Pergamon
Acta Materialia 51 (2003) 1539–1560
Acta MATERIALIA
www.actamat-journals.com

Grain-scale micromechanics of polycrystal surfaces during plastic straining

Dierk Raabe [a,*], Michael Sachtleber [a], Hasso Weiland [b], Georg Scheele [a], Zisu Zhao [a]

[a] *Max-Planck-Institut für Eisenforschung, Max-Planck-Str. 1, 40237 Düsseldorf, Germany*
[b] *Alcoa Technical Center, 100 Technical Drive, Alcoa Center, PA 15069, USA*

Received 3 June 2002; received in revised form 22 November 2002; accepted 26 November 2002

Abstract

This is a study on grain-scale micromechanics of polycrystal surfaces during plastic straining. We use Al–Mg–Si sheets (alloy AA6022) as model material. The work aims at understanding the relationship between microstrain heterogeneity and surface roughness in plastically strained polycrystals in terms of the surface and through-thickness microstructure. Experiments were conducted on polycrystals with identical composition but different processing and microstructures. We performed tensile and bending tests on sheet samples cut in transverse and rolling directions. We investigated the plastic surface microstrains (photogrametry), surface topography (confocal microscopy), particle distribution (metallography, SEM), microtexture (EBSD), and grain size distribution (EBSD) in the same sample regions. We also conducted in-situ straining experiments where the microtexture, surface topography, and stress–strain behavior were simultaneously determined. The results reveal a relationship between the heterogeneity of plastic surface microstrains, roughness, and microstructure. In particular a correlation could be established between microstrains and banded microtexture components (Cube, Goss, {111}[*uvw*]).

Keywords: Aluminium; Texture; Surface structure; Micromechanical modeling

1. Introduction

1.1. Intrinsic surface defects during plastic straining

Plastic straining of polycrystalline metals is accompanied by the gradual development of microstructural surface defects. It is useful in this context to differentiate between *intrinsic* and *extrinsic* defects. As intrinsic ones we denote all surface changes that occur in the form of net residual inhomogeneous surface displacement fields as a result of microstructure dynamics during plastic straining. It is typical of such surface defects that they occur likewise in the bulk. In other words any microstructure phenomenon which gives rise to a heterogeneous displacement inside the bulk upon plastic straining can find its equival-

* Corresponding author. Tel.: +49-211-6792278; fax: +49-211-6792333.
E-mail address: raabe@mpie.de (D. Raabe).

1359-6454/03/$30.00
doi:10.1016/S1359-6454(02)00557-8

ent in a surface defect (e.g. glide steps, shear bands, hard and soft grains, etc.). As extrinsic surface defects we denote all surface changes that occur through the influence of the environment, be it by mechanical contact (forming tools, friction conditions, non-homogeneity of forces and material flows) or by corrosion. These latter effects are not necessarily connected to characteristic microstructure mechanisms which appear likewise in the bulk material. This paper is concerned exclusively with intrinsic surface defects, more precisely, with heterogeneous intrinsic grain-scale surface changes during plastic straining of polycrystalline sheet metals.

Intrinsic surface defects occur at different spatial scales and can have different origin, similar to the corresponding hierarchy of heterogeneous displacement fields caused by lattice defects in the bulk during plastic straining. Figure 1 and Table 1 show some examples of surface displacements in hierarchical order including surface defects generated by elastic distortions (a); point defects (b); atomic slip steps caused by single dislocations leaving the bulk (c); larger crystallographic slip steps created by sets of collectively gliding dislocations on parallel or identical glide planes (d); surface twins or athermal stress-induced transformation phenomena such as martensite (e); non-crystallographic glide traces caused by dislocation bands which contain localized and collective slip activity on parallel and non-parallel glide systems (f); surface cracks (g); orange peel phenomena where crystals at the surface undergo individual out-of-plane displacements (h); individual surface deformation by hard and soft phases (e.g. hard precipitates in a soft matrix) (i); as well as ridging and roping phenomena, which are characterized by the collective deformation of larger sets of similarly oriented grains typically resulting in a banded surface topology (j). Orange peel and ridging phenomena will be addressed in greater detail in the ensuing section. Depending on material and boundary conditions, various types of surface defects can occur at the same time during plastic straining. Elasticity is involved in all cases. From a microstructural standpoint it makes sense to sort the above listed different mechanisms and effects into three basic groups of intrinsic surface defects according to whether they are predominantly governed by point effects, dislocations, or interfaces, similar as in plastically strained bulk material.

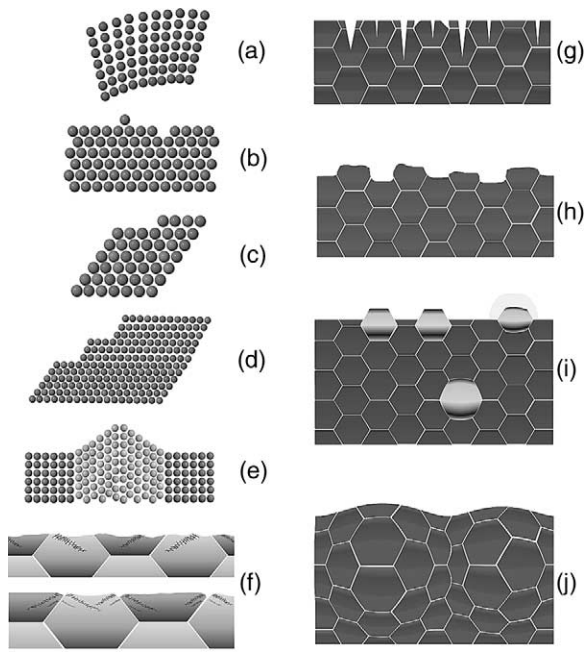

Fig. 1. Some examples of surface defects in hierarchical spatial order (see also Table 1). (a) Elastic distortion; (b) point defects; (c) atomic surface steps caused by single dislocations; (d) larger crystallographic slip steps created by sets of collectively gliding dislocations on parallel or identical glide planes; (e) surface twins or athermal stress-induced transformation phenomena such as martensite; (f) non-crystallographic glide traces caused by dislocation bands which contain localized and collective slip activity on parallel and non-parallel glide systems; (g) surface cracks; (h) orange peel phenomena where crystals at the surface undergo individual out-of-plane displacements; (i) individual surface deformations by hard and soft phases (e.g. hard precipitates in a soft matrix); (j) ridging and roping phenomena, which are characterized by the collective deformation of larger sets of grains typically resulting in a banded surface topology.

1.2. Grain-scale surface defects during plastic straining

Grain-scale roughening in homophase alloys can be grouped into orange peel and banding phenomena. The former are characterized by out-of-plane displacement fields (negative or positive), which roughly map the grain shape of the material. The

Table 1
Hierarchy of surface defects generated during elastic–plastic deformation

Surface phenomenon	Underlying mechanisms	Local surface displacement
Elastic distortions	Local stress state and Hooke's law	$\propto S\,\sigma$
Point defects	Diffusion, mechanics	$\propto a$
Creep pores and hills	Diffusion, mechanics, creep	$\propto \sigma \frac{D\ \ b^3}{(k_B\ T)d^n}$
Atomic slip steps	Dislocations penetrating the surface	$\propto b$
Larger crystallographic slip steps	Dislocation bands consisting of sets of collectively gliding dislocations on parallel or identical glide planes	$\propto M\,\rho\,b\,\mathrm{v}$
Surface twins	Stress-induced orientation dependent twin formation	$\propto \frac{\sqrt{2}}{2}\mathrm{v_z}$
Athermal transformation phenomena	Stress-induced orientation dependent phase transformations (e.g. martensite)	$\propto \frac{\sqrt{2}}{2}\mathrm{v_a}$
Non-crystallographic glide traces	Dislocation bands which contain localized and collective slip activity on parallel and non-parallel glide systems; often related to macroscopic strains	$\propto \epsilon_{\mathrm{pl}}$
Cracks	Fracture mechanics	—
orange peel	Different crystals produce individual out-of-plane grain-scale surface displacements due to their different orientation factors and resulting shape changes	$\propto d\,m\,\epsilon_{\mathrm{pl}}$
Surface co-deformation of hard and soft phases	Hard and soft matter assembled in one microstructure	$\propto R(\sigma_i-\sigma_m)$
Ridging and roping	Collective deformation of larger sets of grains typically resulting in a banded surface topology	$\propto P\ i\ (M_a-M_b)$

b: Burgers vector; a: atomic spacing; S: elastic compliance; σ: stress; M: Taylor factor; ρ: density of mobile dislocations; v: velocity of dislocations; D: Diffusion coefficient (for bulk or grain boundary diffusion); k_B: Boltzmann constant; T: absolute temperature; d: grain size with exponent $-n$, where n is 2 or 3 (bulk or grain boundary creep); $\mathrm{v_z}$: twinned volume of a grain; $\mathrm{v_a}$: athermally transformed volume of a grain; $\epsilon_{\mathrm{pl.}}$ plastic strain; m: Schmid factor; R, P: effective elastic–plastic compliances; σ_i: stress in the inclusion; σ_m: stress in the matrix; i: number of grains in a banded microtexture cluster; M_a: Taylor factor of hard grains in a banded microtexture cluster; M_b: Taylor factor of soft grains in a banded microtexture cluster.

latter are commonly referred to as ridging or roping phenomena. They occur in the form of banded surface undulations which typically extend along the rolling direction of the material. They have a transverse extension above the grain size (Fig. 2).

Grain-scale surface roughening effects have been investigated in various studies, both with respect to the microstructure dependence of wear as well as with respect to the correlation of surface patterning and microstructure. Most recent studies in this field focused on quantitative microstructure experiments with high lateral resolution. Special attention was typically placed on understanding the dependence of surface roughening on grain size, total strain, and crystallographic texture. Early studies showed that surface roughness increases with the von Mises or respectively through-thickness strain and with the grain size [1–8]. At low strains both dependencies were often found to be linear. Increasing deviations from a linear relation were observed at medium and large strains. For instance Wilson et al. [5] found a non-linear dependence of surface roughness on grain size and strain at large plastic strains. Deviations from linearity were also found by Mizuno and Mulki [6]. More recent work on brass, however, revealed a linear dependence of surface roughness on both, strain and grain size up to large strains of 0.8 (logarithmic strain) [8].

Also, a close connection was observed between

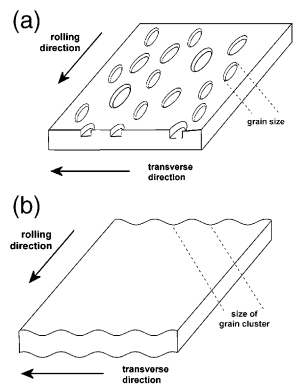

Fig. 2. Grain-scale roughening in homophase alloys occurs in the form of orange peel and banding phenomena. Orange peel is characterized by out-of-plane displacement fields (negative or positive) which roughly map the grain shape. Banding is commonly referred to as ridging or roping. It occurs in the form of banded surface undulations which typically extend along the rolling direction of the material and which have a transverse extension above the grain size.

grain-scale surface roughening and crystallographic texture. More precisely, the microtexture, the misorientation distribution, the two point correlation function, the global texture, as well as individual crystalline shear and reorientation rates were related to grain-scale roughening [5,9–19]. Due to these studies local crystal orientation analysis plays an ever-increasing role in the investigation of surface micromechanics. An important consequence of the close relationship between texture and roughening is that surface micromechanics must be regarded as a tensorial and not a scalar problem [7,20], i.e. the deformation mode has an influence on surface roughness. Vice versa surface topology was observed to have a significant influence on the forming limits of sheet material. For instance Yamaguchi et al. [20] showed that an increase in the forming limits of polycrystalline sheet metals could be achieved by removing surface roughness. The experiments were conducted on balanced biaxial stretching of aluminum sheets and foils. This observation also underlines the close correlation of strain localization, strain hardening, and surface roughness. Similar observations were made by Jain et al. [7] who studied the correlation of strain hardening, grain size parameters, and surface roughening with respect to the prediction of biaxial tensile limit strains of two different aluminum sheets with different strain hardening characteristics. An essential detail of this work is that the use of the average grain thickness as a measure of the grain size served as an excellent parameter to predict the surface roughness during plastic straining.

Mahmudi and Mehdizadeh [8] investigated surface roughening during plastic straining in uniaxial and equi-biaxial stretching experiments using 70–30 brass sheets. Their study substantiated for a wide range of parameters a good correlation between grain size and surface roughness. It was found that the roughness increment was proportional to the applied strain and the grain size of the sheets. Mahmudi and Mehdizadeh observed for all investigated materials that roughness was more pronounced in the transverse direction (referring to the coordinate system imposed by rolling) than in the longitudinal direction. The authors concluded that the non-uniformity of the grain structure, together with the inhomogeneities present in the material, acted as main sources of surface roughening.

Considerable progress towards a more detailed understanding of the micromechanics of grain-scale roughening was achieved by the study of Becker [11] who investigated the effects of strain localization on surface roughness of aluminum sheets employing crystal plasticity finite element simulations. The model accounted for the grain structure near the sheet surface with the behavior of the grains being characterized by a constitutive law which accounts for deformation by crystallographic slip and for rotation of the crystal lattice with deformation. The author found, in addition to the earlier observed linear dependence of surface roughening on strain and grain size, that small-scale strain localization effects at the sheet surface played a significant role for roughening. From this observation he concluded that factors, which affect strain localization, such as strain hardening, texture and microstructure homogeneity, also affect surface roughening. His simulations showed for the first time in a detailed fashion the generation of grain-scale surface patterns induced by the material inhomogeneity inherent in a polycrystal. This study made clear that even in an otherwise homogeneous

portion of material, inhomogeneity generally enters through the presence of grains with different crystallographic orientation.

Lee et al. [12] investigated the development of grain scale roughening (orange peel) in an aluminum 6022-T4 sheet for automotive application by using interference microscopy and electron back scattering diffraction (EBSD) experiments. No clear relationship was identified between orange peel development and the crystallographic orientation of the surface grains. Brass-oriented grains, $\{011\}\langle 211\rangle$ (φ_1=35°, ϕ=45°, φ_2=0°), tended to be located in the high spots or peaks of the surface of the deformed specimen. Surface height gradients predicted from allowing the surface grains to shear in relaxed constraints mode were weakly correlated with the experimental surface height gradient. Bethke et al. [13] presented a similar detailed microtexture study on ridging phenomena in ferritic stainless steel.

Wittridge and Knutsen [14] investigated the evolution of grain-scale surface roughness during uniaxial tensile deformation, placing particular attention on the development of parallel ridges and valleys in aluminum sheets. Their analysis was based on detailed microstructural characterization techniques including polarized light microscopy, bulk texture determination, and microtexture measurements. The authors interpreted the results in terms of in-plane spatial differences in texture at the sheet surface. They found that colonies of the *R* texture component, which were embedded in a matrix with predominant Cube orientation, produced differential straining, which eventually entailed strain localization through the specimen thickness and a ribbed profile. This observation confirmed the fact that grain-scale roughening first produces microscopic strain localization at the sheet surface in the incipient stages of plastic straining and eventually macroscopic through-thickness strain localization. In agreement with earlier work along these lines the authors concluded that ridging phenomena could be attributed to texture inhomogeneity.

One of the most thorough recent studies in the field was published by Baczynski et al. [15] about roping phenomena in an aluminum 6111 automotive alloy. In this work the authors investigated roping and non-roping materials obtained from two different processing routes. In contrast to earlier work their study showed that both ridges and valleys on the upper and lower surfaces were irregularly distributed in the rolling direction, i.e. they were not in synchrony. Ribbed profiles as well as corrugations were only rarely observed. By using electron back scattering diffraction (EBSD) experiments the authors demonstrated that the spatial distribution of Goss oriented grains were mainly responsible for the roping behavior in the investigated alloy. Furthermore, the authors found that the work hardening rates of roping and non-roping specimens were similar. The anisotropy of fracture elongations in the sheet plane was found to be significantly larger in the roping than in the non-roping material. This observation was interpreted in terms of the strong anisotropy of the Goss texture component in the roping material.

Huh and Engler [16] investigated the effects of intermediate annealings on texture and ridging of a 17%Cr ferritic stainless steel. They observed that sheets with weaker through-thickness texture gradients as well as enhanced recrystallization textures were less prone to show pronounced ridging. Similar observations were made by Salsgiver et al. [17]. Engler et al. [18,19] recently presented two detailed reviews on the correlation of ridging and texture in Al–Mg–Si (6xxx) sheet for autobody applications revealing in particular a strong correlation between the orientation density of the Cube orientation and the ridging height.

1.3. Scope of the study

This study investigates correlations between heterogeneous plastic microstrains, microstructure, and both types of intrinsic grain-scale surface effects introduced above (orange peel, ridging/roping). We use a novel experimental approach which is characterized by the joint measurement of accumulated plastic surface microstrains; surface topography; particle distribution; microtexture; and grain size distribution in the same surface areas with high lateral resolution. As model materials we use 6022 aluminum sheets with identical chemical analysis but different

microstructures and different surface roughening behavior.

The goal of this study is twofold. First, we aim at an improved basic understanding of the origin of intrinsic microstructural grain-scale roughening effects, focusing both on individual grain and grain-neighbor mechanics (orange peel) as well as on banded grain-cluster mechanics (ridging). Second, we show that the use of photogrametry for the determination of non-homogeneous surface microstrains can serve as an excellent experimental tool for the correlation of microstructure and micromechanical surface phenomena.

2. Experimental methods

2.1. Specimens and mechanical tests

We used four types of samples of a commercial 6022 aluminum sheet containing 1.2 weight% silicon and 0.6 weight% magnesium. The alloy combines good plastic formability with moderate strength. The sheets were warm rolled, intermediate annealed, cold rolled, and naturally aged to T4 condition using slightly varied process parameters. The sheets had a thickness of 1 mm. As a result all four sample types had the same chemical composition but different surface appearance after 7% plastic straining (engineering plastic tensile strain), due to differences in processing. In the following we denote the samples A, B, C, and D, respectively, according to their individual process history. According to eye-rating samples A showed the smallest and samples D the largest surface roughness after plastic straining in terms of both, the average and absolute roughening height.

On all samples we conducted tensile and bending tests parallel to the rolling and transverse directions. The tensile samples had a dog-bone shape with a width-to-gauge aspect ratio of 6.5. In the bending tests samples were bent over a radius of 7 mm using 10° steps between the measurements. For both types of mechanical tests one set of each sample type was mechanically polished, followed by electropolishing to a mirror finish. Another set remained unpolished to study the transition from inherited to intrinsic surface roughening. The surface topography of each sample was recorded before and after testing in the same surface region. We also conducted in-situ experiments where the microtexture, surface topography and stress–strain curve were simultaneously determined during elastic–plastic tensile straining.

2.2. Measurement of microstrains, surface topography, and microstructure

In the joint experimental investigation all deformed samples were characterized in terms of the accumulated plastic surface microstrains, surface topography, microtexture, grain size distribution, and particle distribution in the same surface and transverse regions between all straining or bending steps, respectively. This means that all correlations between microstrain, microstructure, and surface properties are spatially one-to-one and not statistical.

The plastic surface strains were determined by taking digital gray-scale images of the sample surface after each deformation step. The in-plane and out-of-plane 3D plastic displacement field was then calculated taking the previous or initial state as reference using a photogrametric method. This digital image analysis method is based on the recognition of geometrical changes in the gray scale distribution of images mapping surface patterns before and after straining [21]. Pattern recognition is quantitatively carried out by an image processing method which places a virtual rectangular grid onto the gray scale pixel image. The grid points are characterized by 3D coordinates and by the gray scale distribution in the area surrounding them. After straining the pattern is recognized based on the assumption that the gray scale distribution around a certain coordinate remains constant during straining. From the change in border coordinates containing the correct initial gray scale distribution around a grid point the displacement field is determined for each coordinate. It serves as input for deriving the surface components of the local strain tensor. After each deformation step the surface pattern was acquired and the displacement field as well as the strain distribution were calculated [21].

The 3D surface topography of the specimens

was measured by using a white-light confocal microscope. Confocal microscopy works by a point distance measurement using a depth discrimination method in reflection mode. In a first focusing step light which is emitted from a point source is imaged into the object focal plane of a microscope objective. An in-focus specimen location results in a maximum flux of the reflected light through a detector pinhole (second focusing), whereas light from defocused object regions is partly suppressed. Therefore, the detector signal as limited by the pinhole size is reduced drastically when defocusing the specimen. For the current study this principal design was improved for fast 3D measurements by use of a spinning multiple pinhole mast (Nipkow disk) in an intermediate image plane of a microscope. The Nipkow-disk consists of an array of pinholes arranged in a spiral shape. The disk which is operated in a spinning mode is illuminated by a plane wave and acts as a scanning multiple point light source which is imaged into the object focal plane of the microscope objective. After the reflection of light each illuminating Nipkow pinhole acts as its own detector pinhole. Combined with fast CCD image processing the rotating Nipkow disk affects the in-plane-scan of the object field in video-real-time. Therefore, only the additional out-of-plane scan is required for 3D acquisition. The Nipkow-disk expands the effect of depth discrimination to the area of the microscope object field, which allows optical sectioning like in computer tomography.

Crystal orientation maps at the sample surface were determined by orientation mapping. This is a technique used to analyze local texture and grain boundary topology in crystalline material. Local lattice orientations were measured on a regular grid by automated acquisition and processing of electron backscatter diffraction patterns in the scanning electron microscope. The step size of the measurement grid (15 μm) was chosen as a compromise between accuracy and measuring time. Large areas were measured to identify the microtextures pertaining to long-range surface undulations. From the microtexture data we also extracted the grain size distribution and mapped local grain size cluster phenomena as well as coupled grain size and orientation cluster phenomena. Since it is likely that particularly long range[1] grain-scale surface defects are typically not a consequence of the surface grain layer alone but have their origin in the mechanics of the bulk grains below the surface, we also mapped the microtexture of the transverse sections of all sheets. The scanning area of in the transverse sections amounted to 1200 μm×2000 μm using a step size of 15 μm. The particle density (area percent) was determined by using a digital image analysis method. It was applied to images provided by scanning electron and optical microscopy.

In order to obtain a complete characterization of a polycrystalline surface area the above described experimental procedures were applied after each deformation step to the same strained areas. All sets of mappings, the orientation maps, the topography maps, the surface strain maps, the grain size maps, and the particle distributions were taken over a surface area of about 4000 μm×4000 μm.

3. Experimental results

3.1. Flat tensile tests

3.1.1. Microstrain distribution at the surface

Figure 3 shows the distribution of the accumulated plastic von Mises strain in samples A (best eye-rating), B, C, and D (worst eye-rating) in the surface after 7% plastic straining in the transverse direction (flat tensile test). The in-plane strain distribution was calculated from the displacement field which was determined by use of the photogrametric method explained in the preceding chapter. Sample A reveals a rather homogenous distribution of the von Mises strain with only modest equiaxed localizations in the sheet plane. Strain deviations from the mean value remain small. Pronounced banding of strain does not occur. In contrast, sample B is characterized by strain bands which are aligned along the former rolling direction. The hills and valleys significantly deviate from the mean strain. Sample C also reveals banded microstrains in the rolling direction. However, the differences

[1] Long range meaning *n* times the grain size, where *n* is between 10 and 50.

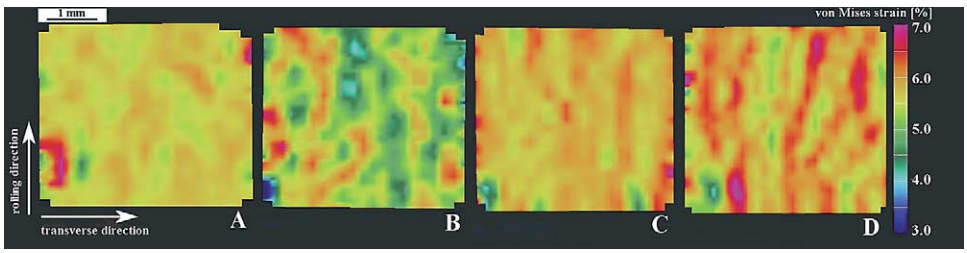

Fig. 3. Distribution of the accumulated plastic von Mises strain in samples A (best eye-rating), B, C, and D (worst eye-rating) in the sheet surface after 7% engineering plastic straining in the transverse direction (flat tensile test). The strain distribution was calculated from the displacement field which was determined by use of a photogrametric method [21].

between valleys and hills are less pronounced than in sample B. The distribution of the accumulated plastic surface strain of sample D reveals pronounced banding in the rolling direction. It is important to note that all samples reveal an alignment of their strain bands *perpendicular* to the macroscopic tension direction (transverse direction when expressed in sheet coordinates) which clearly indicates a microstructural origin of strain localization.

3.1.2. Surface topography after plastic straining

Figure 4 shows the surface topography of samples A–D after 7% engineering plastic tensile strain in the transverse direction. The presented data were taken from samples which were polished to a mirror finish before the tensile tests in order to focus on the intrinsic origin of surface roughening. The figures were assembled using white light confocal microscopy. The color code represents the height of each surface point taking reference to one common minimum at 0.0 μm. The topography maps in the first row have been corrected for undulations stemming from macroscopic sample bending (form correction). The waviness maps in the second row have been filtered for small-scale roughness and show undulations with wavelengths above 0.8 mm. The maps in the third row show the short-range roughness, filtering out all wavelengths above 0.8 mm.

Sample A shows homogeneous roughening. The waviness (second row) is similar as for samples B and C. Short range roughening (third row in Fig. 4) occurs in the form of equiaxed areas of about 20–30 μm in diameter. Most of these grain-shaped roughness peaks and valleys show an absolute roughness value between 2 and 4 μm. The sample does not reveal any particular (longitudinal or transverse) alignment of the roughness pattern (third row). Sample B reveals a much more pronounced surface topography which is characterized by large peaks and deep valleys having both a width of about 1 mm. Sample B also shows pronounced grain scale roughening, however, with larger amplitudes when compared to sample A. Sample C shows banded grain scale roughness parallel to the original rolling direction. The waviness of sample C does not reveal such an orientation dependence. Sample D reveals both, banded long range waviness (second row in Fig. 4) as well as strongly banded grain-scale roughening (third row in Fig. 4). The width of the bands amounts to 200–400 μm. The length of the bands extends in part over the entire scanned area length of 4 mm. This applies equally for the valleys and the peaks. This means that sample D is the only specimen which reveals a banded topology both at the grain scale (third row) and at the grain-cluster scale (second row).

3.1.3. Microtexture

Figure 5 shows the surface microtextures of the four sample types A–D before plastic straining. The data are given in terms of a color-code for the crystallographic axes parallel to the normal direction (ND). The grain structure is revealed by mapping the misorientations among neighboring points. Thin lines indicate orientation changes between 5° and 15° (small angle grain boundaries). Fat lines indicate orientation changes above 15° (large angle grain boundaries). Samples A and B show a very homogeneous grain morphology with

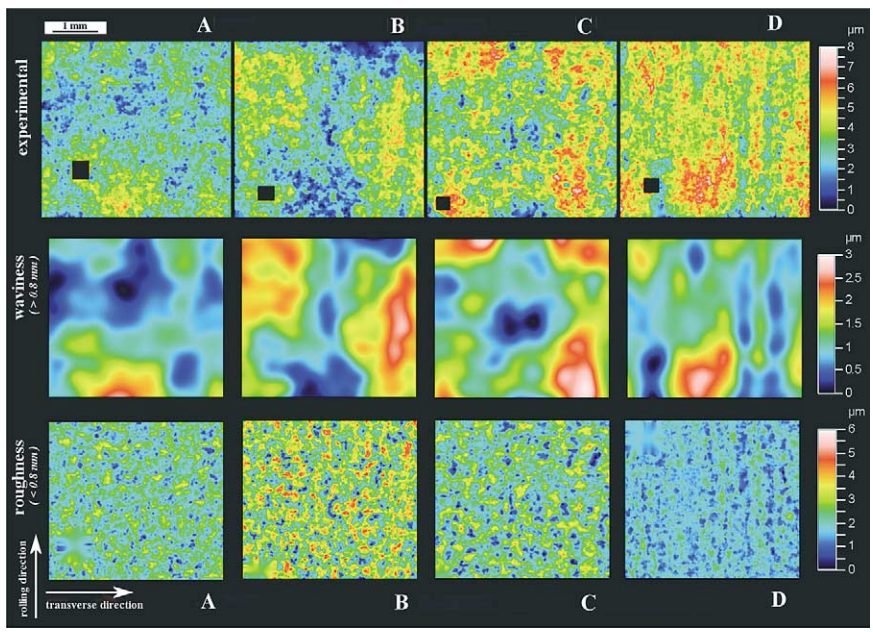

Fig. 4. Surface topography of samples A–D after 7% engineering plastic tensile strain in the transverse direction. The data were taken from samples which were polished to a mirror finish before the tensile tests in order to focus on the intrinsic origin of surface roughening. The figures were assembled using white light confocal microscopy. The color code represents the height of each surface point taking reference to one common point at 0 µm. The topography maps in the first row have been corrected for undulations stemming from macroscopic sample bending (form correction). The waviness maps in the second row have been filtered for small-scale roughness and show undulations with wavelengths above 0.8 mm. The maps in the third row show the short-range roughness, filtering out all wavelengths above 0.8 mm.

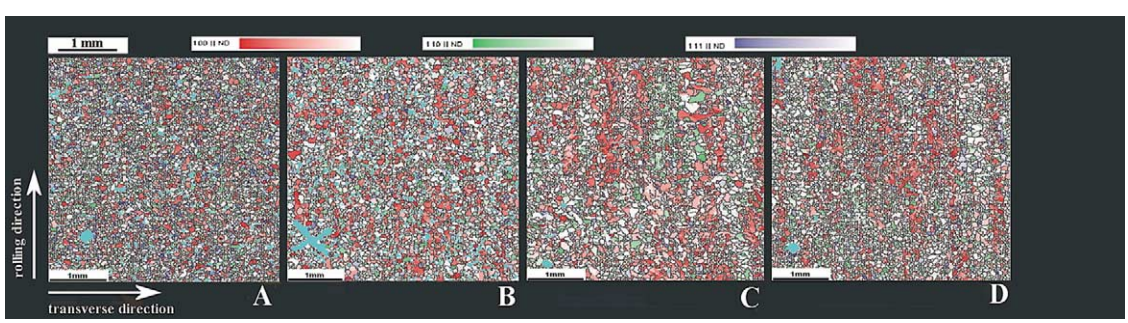

Fig. 5. Surface microtextures before plastic straining. The presentation uses a color code for the crystallographic axes parallel to normal direction (ND). The grain structure is revealed by mapping the misorientations among neighboring measuring points. Thin lines indicate orientation changes between 5° and 15° (small angle grain boundaries). Fat lines indicate orientation changes above 15° (large angle grain boundaries).

randomly distributed texture components. Sample B contains some Cube oriented ($\{001\}\langle 100\rangle$, φ_1=0°, ϕ=0°, φ_2=0°) grain clusters. The microstructures of samples C and D are more heterogeneous in grain morphology, grain size distribution, and microtexture. The latter sample is characterized by in-plane banded clusters of similar crystallographic orientations which are aligned along the rolling direction.

Figure 6 shows the in-plane distribution of some

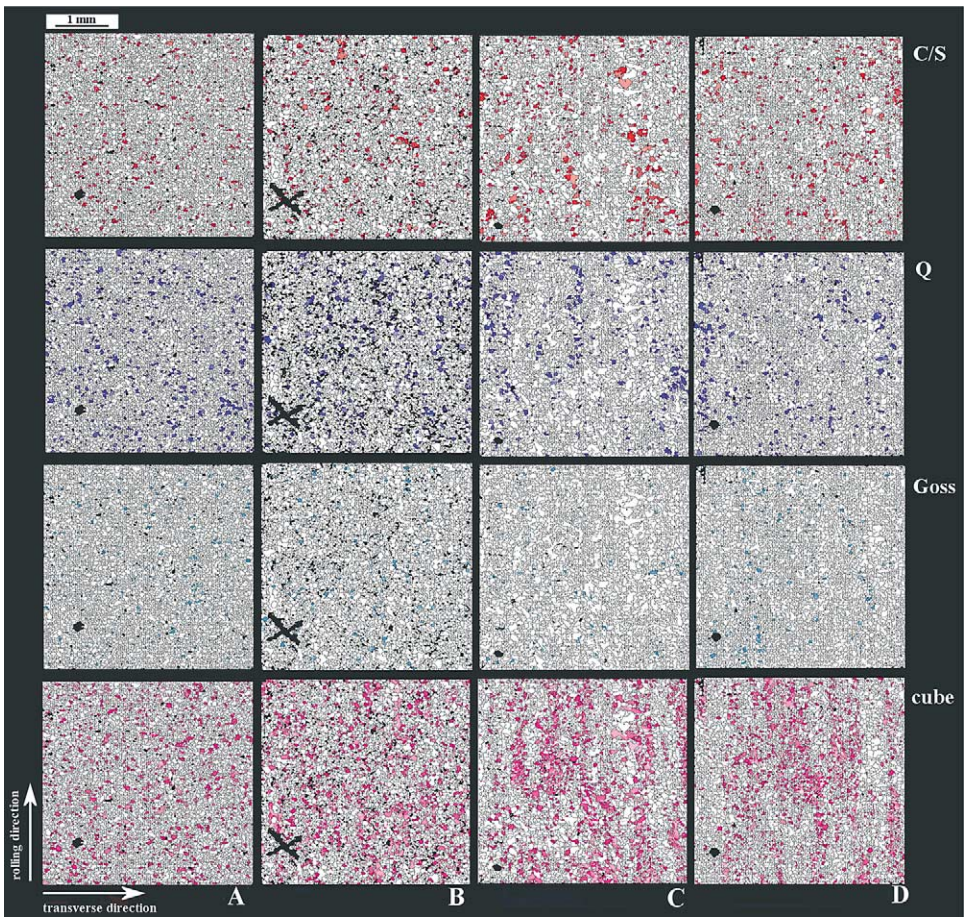

Fig. 6. In-plane distribution of some texture components in the undeformed surfaces. The data show the C/S (C: {112}⟨111⟩, φ_1=90°, ϕ=30°, φ_2=45°; S: {123}⟨634⟩, φ_1=59°, ϕ=34°, φ_2=65°; Q: {013}⟨231⟩, φ_1=45°, ϕ=15°, φ_2=10°; Goss ({011}⟨100⟩, φ_1=0°, ϕ=45°, φ_2=0°), and Cube orientations. The color code indicates the exact orientation in terms of the highest color intensity. Increasing orientation deviation from the exact texture component is indicated by weaker coloring. Deviations beyond 15° are given in white color. The Cube and the Q orientations are recrystallization texture components. The Goss and the C/S components are important rolling texture components.

major orientations in the undeformed surfaces, namely of the C/S (C: {112}⟨111⟩, φ_1=90°, ϕ=30°, φ_2=45°; S: {123}⟨634⟩, φ_1=59°, ϕ=34°, φ_2=65°), Q ({013}⟨231⟩, φ_1=45°, ϕ=15°, φ_2=10°), Goss ({011}⟨100⟩, φ_1=0°, ϕ=45°, φ_2=0°), and Cube texture components. The color code indicates the exact orientation in terms of the highest color intensity. Increasing orientation deviation from the exact texture component is indicated by weaker coloring. Deviations beyond 15° are given in white color. The Cube and the Q orientations are important recrystallization texture components. The Goss and the C/S components are important rolling texture components. Figure 6 substantiates that in samples B, C, and D all texture components are aligned in the form of in-plane orientation clusters parallel to the rolling direction. This applies in particular for the C/S, Q, and Cube orientations among which the latter component occupies the largest area fraction. Banding is strongest in sample D and weaker for samples C and B. Sample A reveals practically no orientation clustering in the rolling direction. The Goss component is (in the surface mappings) less frequent than the other tex-

ture components. However, some Goss oriented grains also occur in weak topological order parallel to the rolling direction in sample D.

Figure 7(a) gives a detailed analysis of the in-plane distribution of the cube orientation and of the ND rotated cube texture component for samples A and D (ND rotated=rotated about the normal direction of the specimen). As in Fig. 6 the color code indicates the exact orientation in terms of the highest color intensity. Increasing misorientation from the exact texture component is indicated by weaker coloring. Deviations beyond 20° are given in white color. The two figures on the right hand side show the in-plane topology of the 10° ND rotated cube texture component (φ_1=0°, ϕ=0°, φ_2=10°) for samples A and D as compared to the arrangement of the exact cube orientation (φ_1=0°, ϕ=0°, φ_2=0°)

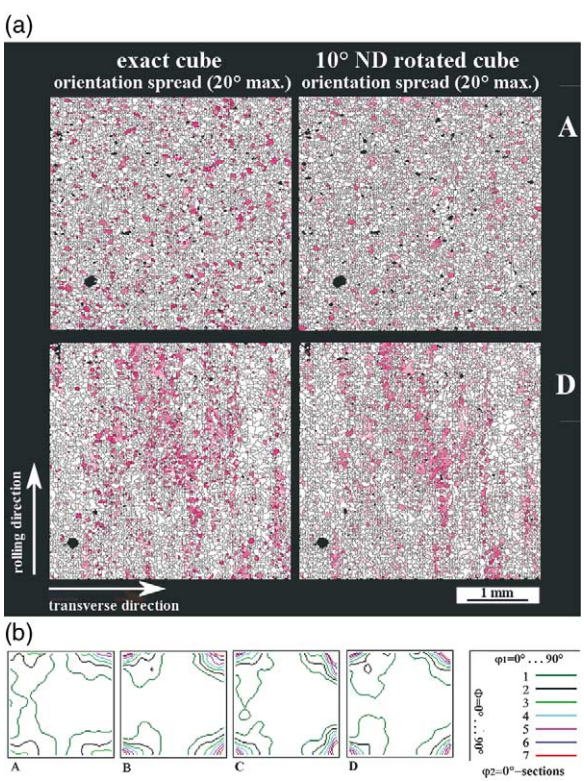

Fig. 7. (a) Mappings of the exact cube component with 20° orientation scatter (left row) and of the 10° ND rotated cube component with 20° orientation scatter (right row) for samples A and D. (b) φ_2=0°-sections taken from the orientation distribution functions for samples A, B, C, and D (textures measured at the sample surfaces by use of EBSD).

(figures on the left hand side). The texture component maps indicate that the 10° ND rotated cube orientation occurs as an individual texture component and not only in the form of the spread of the exact cube orientation [22]. This observation in the microtexture mapping is confirmed by φ_2=0° sections taken from the orientation distribution functions (Fig. 7(b)). All samples show ND rotations of the exact cube orientation. Particularly samples A and B with minimum ridging tendency reveal substantial orientational deviation from the exact cube component about the ND direction (this deviation appears in the form of φ_1 changes in the φ_2=0° sections). Although samples C and D reveal a much sharper cube texture when compared to sample A, they reveal less orientation spread about the ND sample axis.

Figure 8 shows through-thickness (transverse) scans of the microtexture. Although the microtexture is in these mappings less clustered than in the flat sections some correlations between grain morphology and grain size can be observed. Sample A exhibits the most homogeneous grain morphology and grain size of all tested sheets. Sample B shows more heterogeneous grain morphology and grain size with large and non-equiaxed flat grains in the sheet center and smaller grains at the surface. Samples A and B show smaller surface grains than samples C and D. Samples C and D reveal stronger orientation clustering than samples A and B, particularly of the Cube, Goss, and C/S texture components (Fig. 9).

3.1.4. Precipitations

The diameter distribution of the precipitations was measured for all samples (Fig. 10). The data were binned into diameter classes. Class 1 represents the group with biggest and class 13 with the smallest precipitations. Figure 10(a) shows large precipitations with particle diameters between 0.159 μm to 63.096 μm. Figure 10(b) shows smaller particles with diameters between 0.001 μm and 0.3981 μm.

Sample A clearly exhibits the highest area fraction of large precipitations, particularly in the range between 2 μm and 60 μm. The maximum is at class 3, which corresponds to particle diameters between 15.85 μm and 25.12 μm. The other three speci-

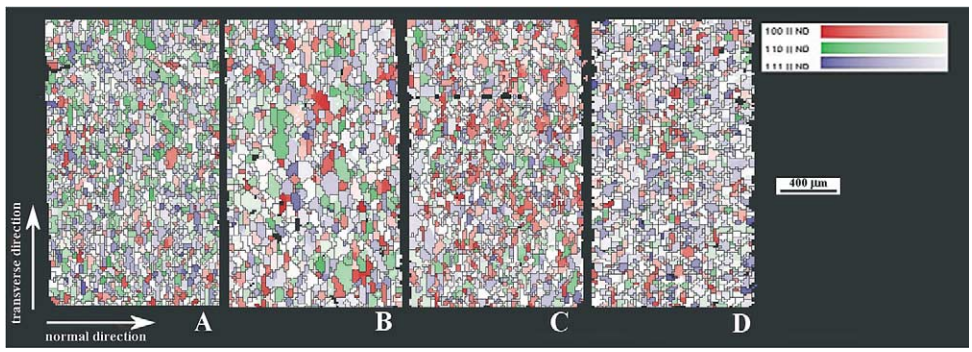

Fig. 8. Through-thickness (transverse) scans of the microtexture in the undeformed samples.

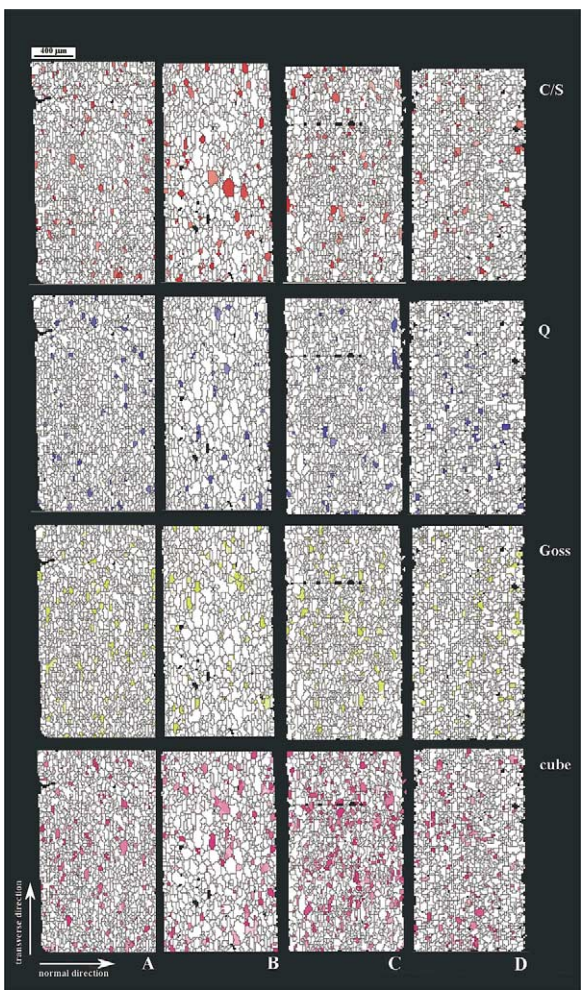

Fig. 9. Through-thickness (transverse) distribution of some texture components in the undeformed samples. The orientations are the same as in Fig. 6.

mens show a much lower share of large particles. This applies in particular to samples C and D. The distribution for the smaller precipitations (Fig. 10(b)) reveals the opposite tendency. Sample D has the largest fraction of fine particles with maxima in classes 5 to 8, which corresponds to particle diameters between 10 nm and 60 nm.

3.2. Bending tests

3.2.1. Microstrain distribution at the surface

Figure 11 shows the von Mises strain distribution as a function of the bending angle. Bending was conducted in rolling and transverse directions using a bending radius of 7 mm (Fig. 11 shows the results in the transverse direction for sample D). The data reveal a rather homogeneous distribution of the equivalent strain along the transverse direction when expressed in sample coordinates (corresponding to the original rolling direction). Minor strain banding can be found parallel to the rolling direction of the original sheet. This direction of the strain bands is the same as observed in the tensile tests for sample D.

3.2.2. Surface topography after plastic straining

Figure 12 shows the evolution of the surface topography during the bending of sample A in 20° steps. The initial banded roughness inherited from cold rolling was not removed prior to the test in order to study the transition from external roughness to intrinsic (microstructural) roughness. Already after 20° bending the initial roughness has ceased to dominate the roughness pattern. Instead, a new intrinsic surface structure appears which is

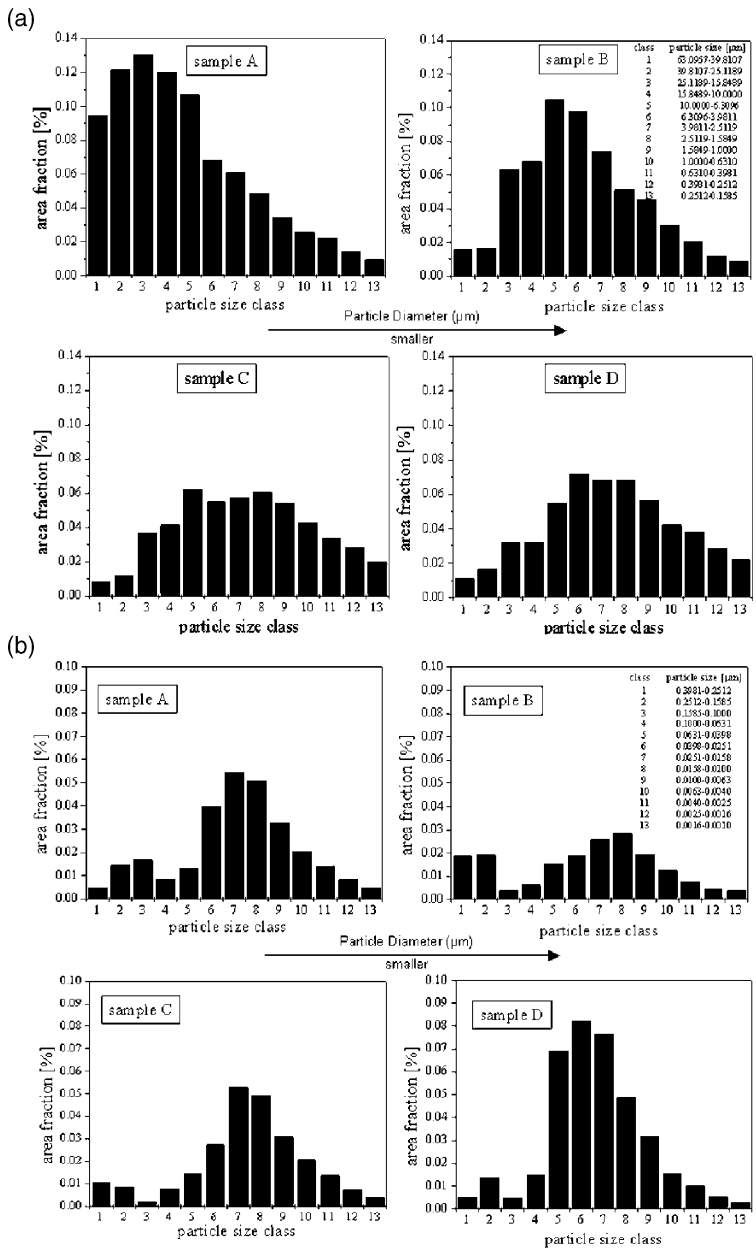

Fig. 10. (a) Size (diameter) distribution of large precipitations with particle diameters between 0.159 µm to 63.096 µm. The data were binned into diameter classes. Class 1 represents the group with biggest and class 13 with the smallest particles. (b) Size distribution of small precipitations with particle diameters between 0.001 µm and 0.3981 µm. Class 1 represents the group with the biggest and class 13 with the smallest particles.

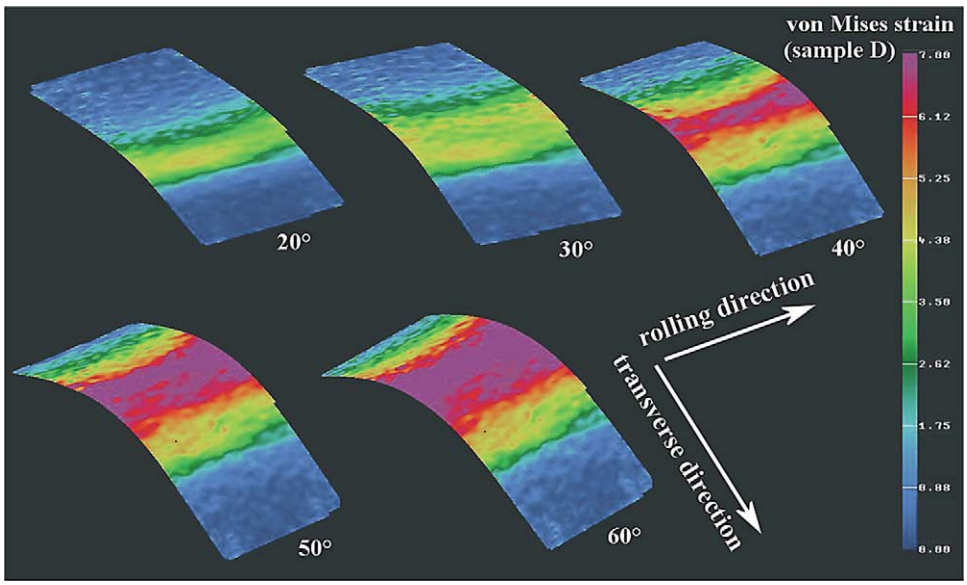

Fig. 11. Von Mises strain distribution in the surface of sample D as a function of the bending angle (bending in the transverse direction of the sheet, bending radius: 7 mm).

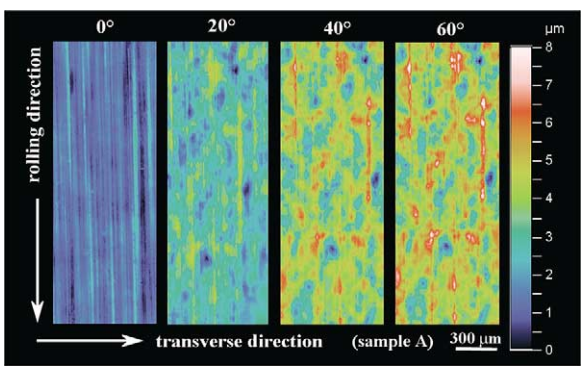

Fig. 12. Evolution of the surface topography during bending of sample A in 20° steps. The initial banded roughness inherited from cold rolling was not removed prior to the test in order to study the transition from external roughness to intrinsic (microstructural) roughness.

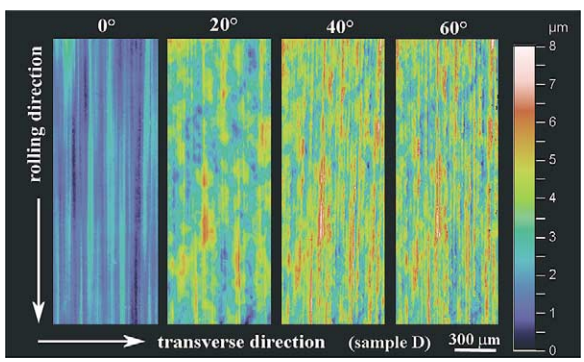

Fig. 13. Evolution of the surface topography during bending of sample D in 20° steps. The initial banded roughness inherited from cold rolling was not removed prior to the test in order to study the transition from external roughness to intrinsic (microstructural) roughness.

characterized by a more equiaxed surface morphology and only a few bands. This surface topography is more similar to orange peel than to ridging. After bending the sample 40° a more elongated roughness pattern appears. After 60° the surface appearance is more dominated by ridging than by equiaxed areas (orange peel). The transverse spacing of the elongated hills and valleys amounts to about 150 µm which is rather large when related to the grain size. The differences in height between the hills (typically around 6 µm) and valleys (typically around 3.5 µm) are rather small. All in all the data show gradual transition from an orange peel type surface pattern at low bending strains to a ridging pattern with low amplitudes and large transverse wavelengths at larger bending strains.

Figure 13 shows the evolution of the surface

topography during bending of sample D in 20° steps. The initial roughness was not removed prior to testing. Already after 20° bending the roughness is characterized by banded surface patterns. Equiaxed valleys and hills are rare when compared to sample A (Fig. 13). Bending the specimen 40° and 60° entails a sharpened ridging profile. The transverse spacing of the hills and valleys amounts to about 5–50 μm which is much smaller than observed in sample A. This value is close to the grain size. The differences in height between the hills (typically around 6 μm) and valleys (typically around 1.5 μm) are larger than in sample A. Altogether the data show a pronounced and narrow ridging pattern with steep transitions between hills and valleys.

Figure 14 shows for all four sample types the initial and the final surface topography after 60° bending (in the transverse direction). The data reveal a gradual transition from an equiaxed pattern resembling orange peel in the case of sample A to sharp ridging in the case of sample D. An essential detail of Fig. 14 is that all four samples reveal similar maximum and minimum values of the sheet normal displacements, but their in-plane

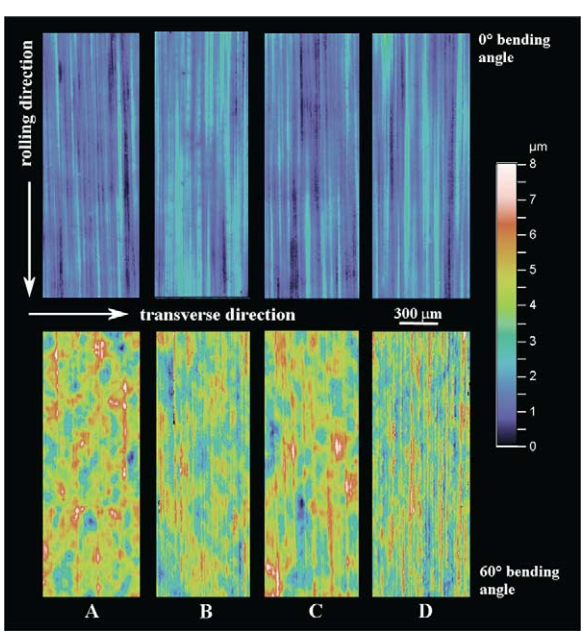

Fig. 14. Initial and final surface topography after 60° bending (in the transverse direction) for all samples.

spatial arrangement, i.e. the pattern of roughening, is dissimilar as stated above. Figure 15 shows the development of the surface roughness for all samples tested in the transverse direction expressed in terms of the surface parameter S_a as a function of the bending angle. This parameter describes the mean absolute deviation from the mean normal displacement,

$$S_a \frac{1}{NM} \sum_{RD=1}^{N} \sum_{TD=1}^{M} |z_{RD,TD}|, \quad (1)$$

where N and M are the number of values in the two perpendicular in-plane axis directions RD (rolling direction) and TD (transverse direction), respectively, and $|z_{RD,TD}|$ are the absolute values of the residual plastic displacements perpendicular to the plane. Figure 15 reveals that all samples show below 30° a linear dependence between the roughness parameter S_a and the bending angle. While samples A, C, and D reveal similar roughening

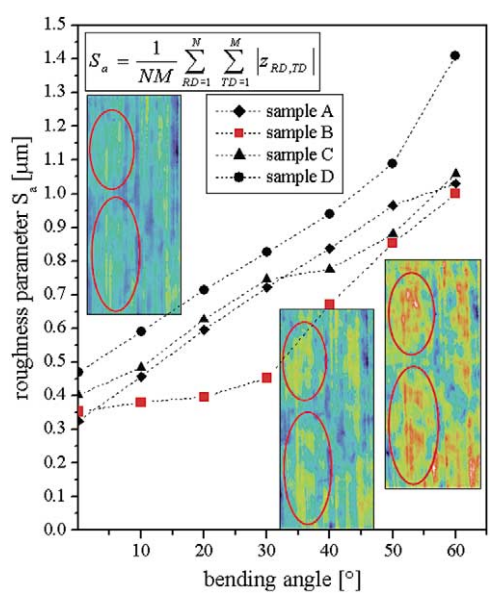

Fig. 15. Development of the surface roughness for all samples tested in the transverse direction expressed in terms of the surface parameter S_a as a function of the bending angle. The S_a value describes the mean absolute deviation from the mean normal displacement (see equation (1)). The surface sections for the development of roughness in sample B are given for 20°, 30°, and 40° bending (transition regime) using the color coding as in Figs 12–14.

behavior also above 30° bending, sample B exhibits a transition in slope at a bending angle of 30°. This fact might at first view indicate a transition in mechanism for sample B. However, the surface sections given for the data points at 20°, 30°, and 40° reveal that the roughness pattern remains nearly self-similar in the transition regime (20°–40°) except for the increase in absolute values. This observation contradicts a change in mechanism.

4. Discussion

Those samples which are characterized by pronounced microtexture banding at the surface (C, D) reveal good correspondence between microstrains, roughness, and microtexture (e.g. Figs 3–5). This means that the observed von Mises microstrain pattern depicted for instance in Fig. 3 for the tensile tests is in part matched by the spatial arrangement of certain texture components. Banded arrays, particularly of Cube and near-Cube texture components, reveal the same spatial wavelength (in the transverse direction) as the observed strain localization pattern. Such correlation was also reported by Engler at al. [18,19]. The Cube and near-Cube components spatially coincide with areas which reveal large out-of-plane displacements (compare Figs 3, 5 and 6). The importance of the spatial arrangement of the Goss texture component for the surface mechanical behavior of the sheets, as reported for a related alloy in an earlier work by Baczynski et al. [15], cannot be directly concluded from the present microtexture mappings taken from the sheet surfaces. Although the Goss texture component is in principle capable of playing an important micromechanical role due to its large Taylor factor and large crystallographic reorientation rate (when strained in transverse direction as in this investigation) its volume fraction in the investigated surface layers is much below that of the Cube orientation. The latter is naturally not anisotropic when rotated 90° about its normal direction (exchange between rolling and transverse direction) owing to its four-fold symmetry. The Taylor factor of the Cube orientation amounts to 2.45 (computed by use of rate-independent Taylor–Bishop–Hill theory) and its rigid-body reorientation rate to 1.0. In comparison, the Goss orientation reveals a large mechanical in-plane anisotropy (nearly a factor of two) both in terms of texture hardness (Taylor factor) and reorientation rate. Its Taylor factor when plastically strained in the rolling direction amounts to 2.45 and its reorientation rate to 0.0. When strained in the transverse direction its Taylor factor is 4.9 and its reorientation rate 2.24.

It must be recalled though that such micromechanical differences between the Goss and the Cube orientation as derived above from homogenization theory do not necessarily match the mechanical behavior of those grains when embedded in a real polycrystal. Tong et al. [23] have shown that the experimentally observed individual deformation response of a particular orientation can deviate from that expected by a Taylor factor associated with average deformation response.

The different kinematical properties discussed here for the Goss and Cube texture components can serve as a good example for a generalized comment on the relationship between texture and ridging. As is apparent from the present data and will also be shown below in terms of crystal plasticity simulations any significant incompatibility in the individual shape change or reorientation rate occurring between abutting clusters of similar crystals or between clusters of similar grains and some average matrix around them is sufficient to initiate a corrugated sheet surface at the scale of the cluster size. It is, therefore, mainly the topological *clustering* and the spacing of crystallographically similar (clustered) regions consisting of kinematically similar grains which entails ridging. Orange peel on the other hand is a grain-scale phenomenon where the overall displacement field is essentially formed by the shape changes of individual grains.

Irrespective of the rather decent spatial correspondence of the Cube orientation (and not of the rare Goss orientation) with the observed microstrain distribution in the surface one must not forget that ridging phenomena which arise from the collective co-deformation of similarly oriented crystals assembled in bands depend also on the *through-thickness* distribution of such texture component clusters (Figs 8 and 9). In other words

it would be misleading to expect a one-to-one correspondence of surface strains, surface topography, and surface texture. In this context one should note that particularly sample C is in the transverse texture sections (Figs 8 and 9) characterized by an orientation density of Goss which is larger than that of Cube. Sample D even reveals substantial through-thickness clustering of a texture component which is close to {111}[*uvw*] (see areas with blue color in Fig. 8), i.e. which is slightly misoriented with respect to the C/S orientation.

Therefore, we conclude that the banded surface topography in samples C and D is basically due to the elongated arrangement of the (slightly inclined) Cube, Goss, and ~{111}[*uvw*] oriented grain clusters in samples C and D both, in the surface layer as well as through the sheet thickness. Particularly the 90° anisotropy of surface roughening (straining in the transverse direction entails larger surface undulations than straining in the rolling direction) can be interpreted in terms of the (weak) presence of the Goss texture component and of the slightly about the ND (normal direction) rotated Cube component which both reveal a significant anisotropy in Taylor factor and reorientation rate whilst the exact Cube orientation is symmetrical with respect to this operation.

Weaker correlation between the measured microstrains and the in-plane surface texture is observed for samples with less pronounced texture banding. For instance, samples A and B reveal a microtexture with no elongated orientation arrays and, consequently, with smooth roughening behavior. However, the in-plane distribution of the accumulated plastic strain at the surface is less homogeneous than the surface microtexture suggests. For instance, Fig. 3 shows pronounced banded strain localization effects for sample B, although with a larger transverse spacing of the strain maxima than in samples C and D, whilst its corresponding surface texture appears to be homogeneous (Fig. 5). This discrepancy can be explained in terms of the through-thickness distribution of the Cube and particularly of the Goss grains (Figs 8 and 9). The result also shows that the direct determination of surface microstrains is a more sensitive, direct, and tractable investigation tool for surface micromechanics than texture measurements or roughness measurements alone.

Interesting details about the correlation between microstrains and microstructure are also in Figs 12 and 13. Sample A (Fig. 12) reveals after bending an equiaxed orange peel-type surface roughness pattern. The valleys and hills have diameters between one and four times the grain size. This pattern resembles the situation presented in Figs 1(h) and 2(a). The banded structures, which are initially present at the surface, are rolling marks, i.e. extrinsic surface defects inherited from rolling. They do not have intrinsic microstructural origin. Sample A does not seem to change its basic intrinsic surface behavior during straining, i.e. the mechanisms and the resulting surface pattern remain the same throughout the straining history. Roughness increases linearly as a function of strain, i.e. of the bending angle (Figs 11 and 15).

Sample D shows a different roughening behavior than sample A (Fig. 14). For small bending angles up to 20° sample D exhibits an orange peel behavior similar to sample A (Fig. 12). Above 20° bending the roughness pattern changes from an equiaxed topology into a more elongated banded structure which rapidly becomes sharper with increasing strain. Three important observations can be made from these figures: First, the *slope* or *change* in slope of the surface roughening parameter S_a as a function of strain or respectively bending angle does not provide reliable insight into the basic microstructural mechanism behind roughening. This observation was already made when describing the roughness maps of sample B in Fig. 15 in the preceding section. In this case (sample B) the slope of the scalar roughness parameter S_a changed without any significant topological match in the surface roughening pattern. In the present case of sample D, changes in surface pattern at a bending angle of 20° (Fig. 13) are not matched by a corresponding change in slope of S_a. Second, the *absolute* value of roughening does not indicate which mechanism prevails. In other words strong roughness can originate from both, orange peel or ridging. Third, eye rating of surface quality does not necessarily reflect the value of the scalar roughness parameter S_a which characterizes a sample surface. It is more likely that eye rating of sur-

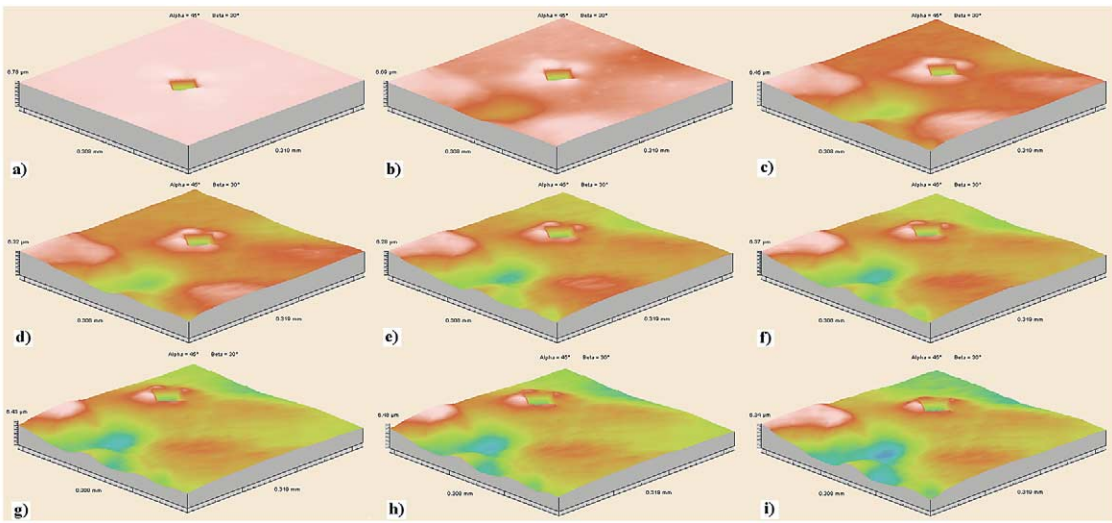

Fig. 16. Subsequent images of grain-scale roughening from an in-situ experiment. The data were directly observed during a flat tensile test in a white light confocal microscope. The data show the strong orientation dependence of grain scale surface roughening. While two grains reveal a positive displacement parallel to the sheet normal the small grain between them reveals the opposite behavior (when using the displacement of the large grain as a reference).

face roughness is much more influenced by the type of pattern which appears rather than only by the absolute values of the sheet normal displacements. In this context ridging with its elongated sharp surface lines seems to be more critical to the human eye than the equiaxed orange peel type surface pattern.

Figures 16 and 17 give an in-situ example of the dependence of orange peel surface roughening on the local grain orientation. The roughness data were directly observed during a flat tensile test in the white light confocal microscope. The data show

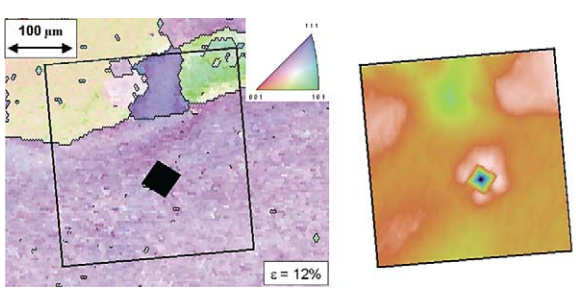

Fig. 17. Surface microtexture map (left hand side) together with the roughness map after 12% engineering plastic straining taken from the in-situ experiment. The square in the center represents the indent which was used as a marker.

the strong orientation dependence of surface roughening at the grain scale. While two grains reveal a positive displacement parallel to the sheet normal the small grain between them reveals the opposite behavior (when using the displacement of the large grain as a reference).

Detailed theoretical studies on the shape change of grains at the surface of polycrystal aggregates were conducted using viscoplastic crystal plasticity finite element simulations. Figure 18 shows some results obtained from simulations of a plastically stretched bamboo polycrystal which consists of three subsequent crystals. The two outer grains have Cube orientation. The grains in the middle have Goss orientation (Fig. 18(a)), 90° about the normal rotated Goss orientation (Fig. 18(b)), and *S* orientation (Fig. 18c). The simulations show the grain-scale evolution of differences in surface topology during longitudinal straining. The Goss orientation has similar kinematic properties to the Cube component when stretched in the longitudinal direction. When rotated 90° about the normal direction as in Fig. 18(b) (to simulate transverse straining of the bamboo polycrystal with the Goss component in the middle), the Goss orientation (now 90° rotated) is much harder than the Cube

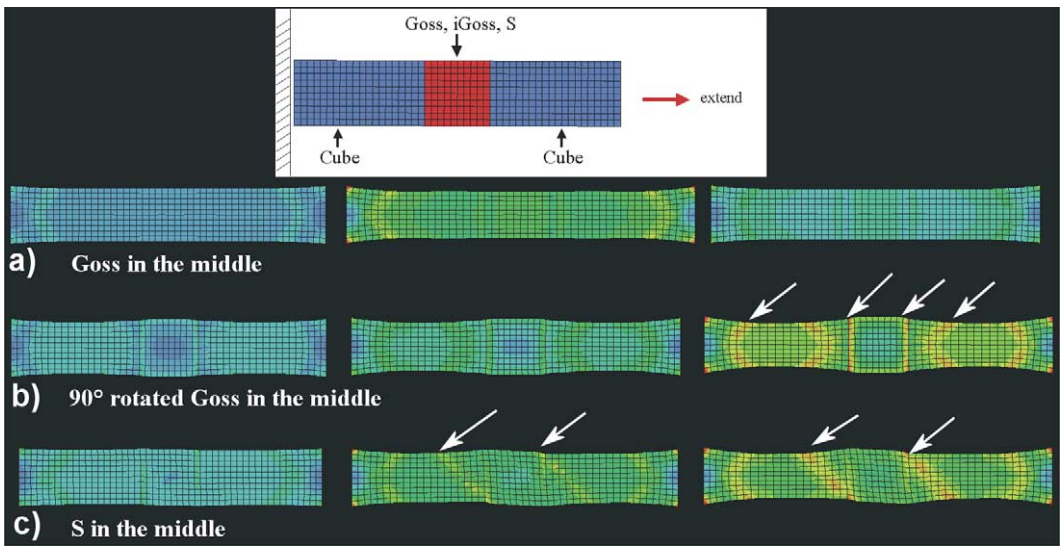

Fig. 18. Crystal plasticity finite element simulations of a plastically stretched bamboo polycrystal which consists of three subsequent crystals. The two outer grains have Cube orientation. The grains in the middle have Goss orientation (Fig. 18(a)), 90° about the normal rotated Goss orientation (Fig. 18(b)), and *S* orientation (Fig. 18(c)). The arrows indicate strain localization. The colour code indicates the von Mises strain.

orientation and, therefore, retains a higher surface level than the cube orientation. The interface between the crystals is characterized by strong strain localization effects. Such localization phenomena are usually regarded as starting points for ridging [11,24]. Strain localization in the form of shear banding (45° with respect to the sample surface) is even initiated inside the (Cube) grains for the co-deformation of the *S* and the two Cube crystals (Fig. 18(c)). The simulations clearly show that the displacement mismatch between two neighboring crystals is sufficient to initiate strain localization. The mismatch among abutting crystals entails steep changes of the out-of-plane displacement field across the grain boundary which in turn leads to large local stresses, similar as for cracks, and, therefore, to strain localization. This kinematical effect of microtexture on the early stages of strain localization was also pointed out by Becker [11]. The largest incompatibility is observed for Cube and 90° rotated Goss (corresponding to a grain pair consisting of Cube and Goss when strained in the transverse direction). The second largest incompatibility occurs for Cube and *S*. Cube and Goss are very compatible when strained in the longitudinal direction, and, consequently, do not reveal strain localization.

The microtexture measurements also revealed differences in grain size and grain shape in the sheet plane (Fig. 5) as well as through the sheet thickness (Fig. 9). Samples A and B show smaller surface grains and only very few clusters of similar oriented grains. Samples C and D show a much more heterogeneous distribution of the grain size and shape. In particular they reveal clusters of similarly oriented crystals which are aligned along the former rolling direction of the sheets. This indicates that groups consisting of similarly oriented grains might have been formed during processing from originally uniform larger grains which were elongated in the rolling direction for instance in the former hot band. This process might occur by discontinuous simultaneous nucleation of similarly oriented new grains in one original hot band or cold band grain or by continuous subgrain coarsening. Figure 19 gives a closer view on this aspect. It shows the grain boundary misorientations in a flat section at the surface for samples A and D. While sample A contains mainly large angle grain boundaries with misorientations above 25° (black lines), sample C shows larger areas where neighb-

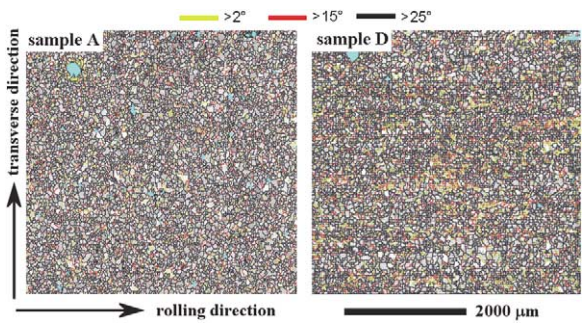

Fig. 19. Grain boundary misorientations in a flat section at the surface for samples A and D. Sample A contains mainly large angle grain boundaries with misorientations above 25° (black lines). Sample D shows more small angle misorientations between 2° and 15° (yellow lines).

oring grains have small angle misorientations between 2° and 15° (yellow lines). This observation suggests that the grain structure of sample A might have been created essentially by discontinuous subgrain coarsening, i.e. by classical formation of large angle boundaries, and that sample D contains areas (containing large fractions of yellow lines) which have essentially undergone continuous subgrain coarsening [25].

This suggestion is also covered by Fig. 20 which shows the misorientation distributions for the in-plane microstructures of samples A and D. The corresponding distributions of the rotation axes are not given. The two figures in the left column show the point-to-point misorientation distributions for all pairs of neighboring microtexture measurement points (Fig. 5). This kind of presentation is also referred to as *correlated* misorientation distribution. The two figures in the right column show the statistical misorientation distributions for random pairs of non-neighboring microtexture measurement points. This kind of presentation is also referred to as *uncorrelated* misorientation distribution. Minor in-grain misorientation scatter below 2° is not given in the diagrams. The black lines in all diagrams show the misorientation function for the case of a *random* theoretical crystallographic misorientation distribution.

Comparing the correlated (neighbor pair) misorientations (left hand side of Fig. 20) of sample A and D clearly reveals that the distribution for sample A resembles that of a random misorientation distribution. In other words the microstructure of sample A does not contain significant grain clustering or misorientation correlations beyond the statistical limit. In contrast to this observation sample D reveals a much larger volume fraction of small angle grain boundaries which exceeds the statistical limits particularly in the regime between 2° and 25°. Large angle grain boundaries with misorientations above 25° have a frequency much below the statistical limit. Furthermore, the diagrams on the right hand side of Fig. 20 reveal that the characterization of grain clustering must be conducted by using a point-to-point misorientation analysis of actual *neighbor* pairs rather than an uncorrelated misorientation analysis of statistical pairs of orientations. This means that a reliable grain cluster analysis requires the use of microtexture data.

In the context of grain cluster analysis (Figs 19 and 20) it is also important to consider the possibility of particle-stimulated nucleation [19,22,26]. The samples which show the most random microtextures with very rare orientation clustering (Fig. 5) are the ones which have the largest area fractions of large particles (Fig. 10(a, b)). These are known to stimulate particle-stimulated nucleation and, thereby, contribute to topological texture randomization entailing a drop in ridging [19,22,26]. This is confirmed by the strong pronunciation of the 10° ND rotated Cube orientation in samples A and B which can be taken as an indicator for particle-stimulated nucleation in these samples (Fig. 7(a,b)).

5. Conclusions

The study presented a joint experimental investigation on the relationship between plastic microstrains, surface topography, and microstructure (particles, texture, grain size) during plastic straining of aluminum sheets of different processing. The main conclusions are:

Changes in intrinsic surface topography during plastic straining can in detail be understood in terms of the distribution of the accumulated plastic microstrains, which in turn depend on the in-plane

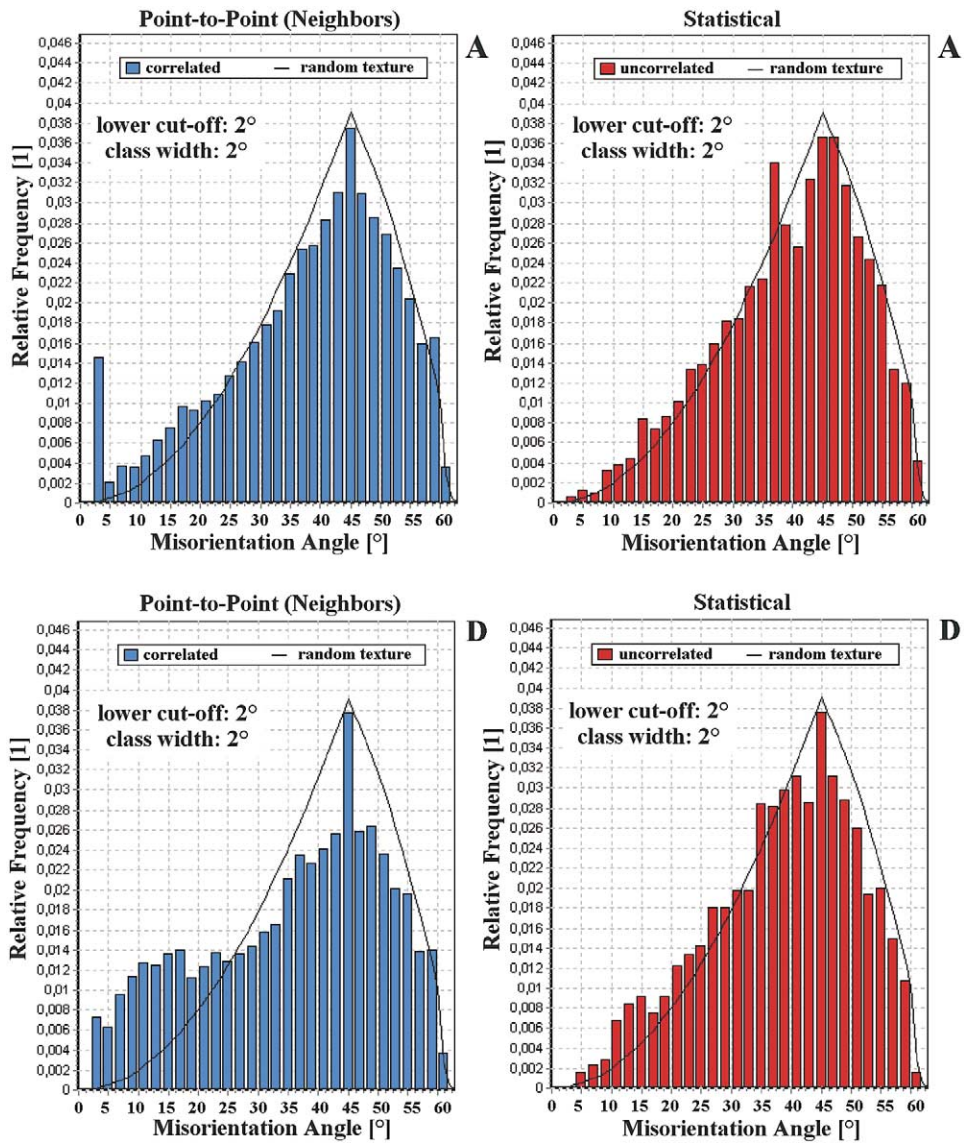

Fig. 20. The two figures in the left column show the point-to-point misorientation distributions for all pairs of neighboring microtexture points (correlated misorientation distribution). The two figures in the right column show the statistical misorientation distributions for random pairs of non-neighboring microtexture points (uncorrelated misorientation distribution). The black lines in all four diagrams show the misorientation function for the case of a random crystallographic texture.

and through-thickness microstructure. The determination of microstrains gives a clearer picture of surface micromechanics than texture and grain size measurements alone.

The in-plane and through-thickness distribution of Cube, Goss, rotated Goss, and {111}[*uvw*] (close to C/S) microtexture components can explain the observed accumulated plastic microstrains and resulting surface topographies.

Ridging is promoted by the presence of grain clusters consisting of the above-mentioned components. The joint occurrence of soft and hard clus-

ters (e.g. Cube and Goss or, respectively, transverse Goss) stimulates strong heterogeneity of surface strains and entails ridging.

Grain clustering can be viewed as a grain boundary problem which is characterized by the occurrence of large fractions of small angle grain boundaries, particularly between 2° and 25°, among neighboring crystals and of small fractions of large angle grain boundaries above 25° misorientation.

Orange peel was explained in terms of the deformation behavior of individual crystals using in-situ experiments and crystal plasticity finite element simulations. It was found that particularly the grain neighborhood is important for surface roughening and early stages of strain localization. Strain localization can be initiated inside grains as well as at grain boundaries depending on the orientations of the abutting surface crystals.

The presence of large precipitates leads to more homogeneous microstructures and more random microtextures. Such microstructures have a smaller tendency to undergo pronounced ridging or orange peel roughening.

Acknowledgements

The authors are grateful to T. Rouns at Alcoa Technical Center for his work on precipitations.

References

[1] Mietzner K. Stahl und Eisen 1961;81:950.
[2] Kienzle O, Mietzner K. Atlas Umgeformter Metallischer Oberflächen. Berlin, Germany: Springer-Verlag, 1967.
[3] Osakada K, Oyane M. Bull JSME 1971;14:171.
[4] Fukuda M, Yamaguchi K, Takakura N, Sakano Y. J Japan Soc Technol Plasticity 1974;15:994.
[5] Wilson DV, Roberts WT, Rodrigues PMB. Metall Trans 1981;12A:1603.
[6] Mizuno T, Mulki H. Wear 1996;198:176.
[7] Jain M, Lloyd DJ, MacEwen SR. Int J Mech Sci 1996;38:219.
[8] Mahmudi R, Mehdizadeh M. J Mater Proc Techn 1998;707:80–1.
[9] Takechi H, Kato H, Sunami T, Nakayama T. Trans JIM 1967;8:233.
[10] Chao H-C. Trans ASM 1967;60:37.
[11] Becker R. Acta mater 1998;46:1385.
[12] Lee PS, Piehler HR, Adams BL, Jarvis G, Hampel H, Rollett AD. J Mater Proc Techn 1998;80–81:315.
[13] Bethke K, Hölscher M, Lücke K. Mater Sci Forum 1994;157:1137.
[14] Wittridge NJ, Knutsen RD. Mat Sc Engin 1999;A269:205.
[15] Baczynski GJ, Guzzo R, Ball MD, Lloyd DJ. Acta mater 2000;48:3361.
[16] Huh M-Y, Engler O. Mat. Sc. Engin 2001;A308:74.
[17] Salsgiver JA, Larsen JM, Borneman PR. In: Chandra T, editor. Proceedings of the International Conference on Recrystallisation ‘90. Warrendale, PA: The Minerals, Metals and Materials Society, TMS; 1990. p. 849–54.
[18] Engler O, Brünger E. Mater Sc Forum 2002;396–402:345.
[19] Engler O, Hirsch J. Mat Sc Engin 2002;A336:249.
[20] Yamaguchi K, Takakura N, Imatani S. J Mater Proc Techn 1995;48:27.
[21] Raabe D, Sachtleber M, Zhao Z, Roters F, Zaefferer S. Acta Materialia 2001;49:3433.
[22] Engler O, Mülders B, Hirsch J. Z Metallkunde 1996;87:454.
[23] Tong W, Hector LG, Weiland H, Wieserman LF. Scripta Met 1997;36:1339.
[24] Korbel A, Embury JD, Hatherly M, Martin PL, Erbslöh HW. Acta metall 1986;4:1999.
[25] Humphreys JF, Hatherly M. Recrystallization and related annealing phenomena. Pergamon Press, 1995.
[26] Beaudoin AJ, Bryant JD, Korzekwa DA. Metallurgical and Materials Transactions A 1998;29:2323.